Title
Miniature ion thruster ring-cusp discharge performance and behavior

Journal
Journal of Applied Physics, 122(24)

ISSN
0021-8979

Authors
Dankongkakul, Ben
Wirz, Richard E

Publication Date
2017-12-28

DOI
10.1063/1.4995638

Peer reviewed

Miniature ion thruster ring-cusp discharge performance and behavior

Ben Dankongkakul[a] and Richard E. Wirz[b]
University of California, Los Angeles, 420 Westwood Plaza, 90064 California, USA

(Received 12 July 2017; accepted 11 November 2017; published online 27 December 2017)

Miniature ion thrusters are an attractive option for a wide range of space missions due to their low power levels and high specific impulse. Thrusters using ring-cusp plasma discharges promise the highest performance, but are still limited by the challenges of efficiently maintaining a plasma discharge at such small scales (typically 1–3 cm diameter). This effort significantly advances the understanding of miniature-scale plasma discharges by comparing the performance and xenon plasma confinement behavior for 3-ring, 4-ring, and 5-ring cusp by using the 3 cm Miniature Xenon Ion thruster as a modifiable platform. By measuring and comparing the plasma and electron energy distribution maps throughout the discharge, we find that miniature ring-cusp plasma behavior is dominated by the high magnetic fields from the cusps; this can lead to high loss rates of high-energy primary electrons to the anode walls. However, the primary electron confinement was shown to considerably improve by imposing an axial magnetic field or by using cathode terminating cusps, which led to increases in the discharge efficiency of up to 50%. Even though these design modifications still present some challenges, they show promise to bypassing what were previously seen as inherent limitations to ring-cusp discharge efficiency at miniature scales. *Published by AIP Publishing.* https://doi.org/10.1063/1.4995638

I. INTRODUCTION

Ion thrusters are a highly efficient form of in-space propulsion that can be used for high ΔV orbit station keeping and as a primary propulsion system for deep space missions. Miniature ion thrusters (typically 1–3 cm diameter) are an attractive option for secondary propulsion for larger spacecraft, for formation flying and attitude control, or for primary propulsion to execute orbit transfers and maintenance in smaller spacecraft.[1–3] To date, discharges using ring-cusp designs have exhibited the best efficiency for ion thrusters at all scales.[4] However, smaller ion thrusters exhibit relatively low discharge efficiencies due to the inherent increase in the surface area-to-volume ratio of the plasma generation (i.e., discharge) chamber.[5]

Ring-cusp ion thrusters typically use samarium cobalt permanent magnets to produce strong and relatively short-ranged magnetic fields for an efficient confinement of the discharge plasma. Placed in alternating polarity, these magnets provide strong cusp boundaries near the walls to confine the plasma while the bulk plasma remains effectively unmagnetized and thus, well suited for uniform plasma generation and beam flatness. Since the cusp magnetic fields can be approximated as boundary-only effects, most design efforts of conventional scale ring-cusp ion thrusters have relied on analytical models[6,7] and semi-empirical treatment of cusp confinement physics.[8,9] For example, plasma losses to the cusp are estimated using the semi-empirical hybrid leak width and concepts such as the highest closed magnetic field contour are used as a design figure-of-merit and for discharge models.[7,10] This approach has worked well for larger ion thrusters, however, these design principles become difficult to implement at the miniature scale as the cusp fields are no longer localized to the discharge boundary. In fact, the ring cusps produce complex and strong B-field structures that dominate most of the chamber volume.

To investigate and improve miniature ion thruster performance, a complete experimental examination of the discharge chamber would provide critical insights into the discharge plasma behavior at these reduced scale lengths. Therefore, the objective of this paper is to use a complete discharge map of key plasma parameters to understand the discharge plasma behavior and its relation to the performance as an ion thruster or ion source. The key plasma parameters of interest include the electron energy distribution functions (EEDFs) for both high energy (primary) and low energy (plasma) electrons, as well as plasma density and potential. The 3 cm Miniature Xenon Ion (MiXI) thruster is used as the platform to test several magnetic fields and discharge configurations. The performance data are obtained using a simulated ion thruster operation at several discharge conditions. A complete EEDF and plasma parameter map for each configuration is obtained using a Langmuir probe and analyzed in conjunction with the performance data.

Since conventional DC ring-cusp ion thrusters already have the highest efficiencies of any well-developed electric propulsion technology, there has been little motivation to map the internal plasma. To date, only a handful of authors have attempted to acquire a partial or full map of the plasma structure within an ion thruster discharge chamber. Many researchers have used various probes to measure the plasma properties at sparse locations to characterize the overall performance. Herman and Gallimore[11] partially mapped the plasma parameters as well as generated EEDF curves inside the 30 cm NASA Solar Technology Application Readiness (NSTAR) ion thruster in the region near the hollow cathode

[a]Electronic mail: bendankongkakul@ucla.edu
[b]Electronic mail: wirz@ucla.edu

and the grid system. Hubble *et al*. obtained a detailed spatial distribution map of the plasma density inside an inverted cusp structure with a helium afterglow plasma using laser collisional induced florescence (LCIF).[12] Tsukizaki *et al*.[13] used both Langmuir and optical probes through the grid system to measure a coarse plasma parameter map of the μ-10 ECR ion thruster. Mao and Wirz[14] have provided the only effort to fully map a miniature (3 cm) ring-cusp discharge and the results showed highly structured and non-uniform plasma density contours. However, the discharge was not designed as an ion thruster and their results did not include an EEDF map. Previous to this work, a full plasma parameter or EEDF map of a ring cusp discharge has not been obtained. These results are crucial to resolving the primary electron population within the discharge chamber as they are known to dominate the discharge behavior at the miniature-scale.[15]

II. APPROACH

Several sets of experimental measurements and analyses were conducted to characterize the performance and discharge structure for three different discharge configurations. This section begins with a description of the test facility and various components of the MiXI thruster. The magnetic field topology for each of the three discharge configurations is then discussed along with the design intention of each subsequent configuration. Next, this section describes the methodology used for obtaining the simulated performance and discharge mapping data, including the necessary assumptions and the approached used for the Langmuir probe analyses. The section ends by describing an analysis procedure used to calculate the various species interaction rates based on the plasma properties and the associated collision cross-sections.

A. Experimental setup

The experiments were conducted inside a 20″ diameter by 36″ height bell-jar vacuum chamber at the UCLA Plasma & Space Propulsion Lab. The cryopump vacuum system provides a base and an operating pressure of 2×10^{-6} Torr and less than 5×10^{-5} Torr, respectively. Xenon gas was injected into the chamber through an electrically isolated gas feed line. Probes were mounted onto a set of orthogonally mounted linear stages configured to raster along an azimuthal slice of the discharge chamber.

The original MiXI thruster, diagrammed in Fig. 1, was used as a modifiable platform to test the various magnetic field configurations. The thruster has a 3 cm diameter by 3 cm length aluminum discharge chamber and the xenon gas propellant was injected through an annular porous-metal gas injector located at the upstream end of the discharge chamber. The MiXI grid system "Small Hole Accelerator Grid" (SHAG) optics improve the neutral confinement (~5%) while maintaining high ion transparency (~75%). The steel side pole piece improves the downstream ring cusp geometry by pulling the field lines closer to the walls toward the grids. The miniature discharge hollow cathode was replaced with a 5 mil tungsten filament cathode to simplify operation and reduce noise in the probe measurements. The filament is ~2.5″ in the total uncoiled length and is typically heated with 18 to 20 W of

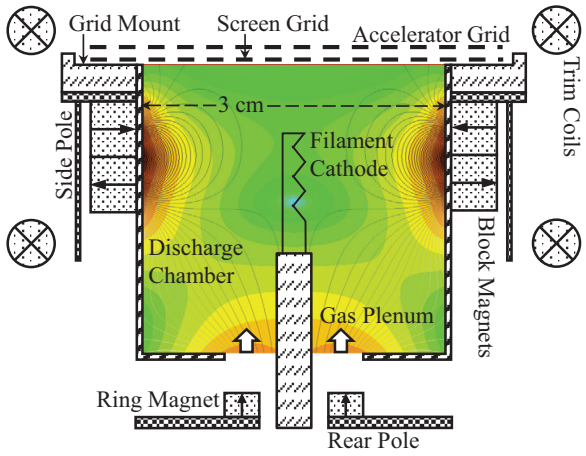

FIG. 1. Diagram of the 3 cm diameter MiXI thruster (not to scale) with the key components labeled and overlaid onto the magnetic field contour (in logarithmic scale).

power. A set of trim coils was added to allow *in-situ* changes to the magnetic field, particularly within the center region of the chamber, where the fields are the weakest. A thermocouple was attached to the outer wall of the side pole piece.

The thruster was operated without ion beam extraction in which the discharge cathode was grounded to the vacuum chamber. Figure 3 shows a simplified wiring diagram of the MiXI thruster and power supplies required for plasma generation and measurement of the discharge properties. For some configurations, a secondary or tertiary discharge power supply was wired to the rear plate or internally isolated ring electrodes to segment the chamber surfaces. The cathode heater supply generates between 8 to 12 V across the filament during normal operation. The negative terminal of the cathode heater supply was wired to the discharge supply to ensure that primary electrons did not gain excessive energies relative to the discharge voltage. In addition, the filament was installed in a manner that primary electrons created further upstream had higher energies than those created at the tip of the filament—a characteristic more similar to hollow cathode operation.[16]

All measurements were recorded using a DAQ module that featured a 300 Vrms channel-to-channel isolation. The power supply voltage and current values were measured directly and through a shunt resistor, respectively. The Langmuir probe voltage sweeps were generated in LabVIEW and amplified using a Kepco BOP-100m bipolar amplifier. The Langmuir probe current was measured through a 32 Ω shunt resistor on the high side of the power supply to avoid the leakage current in the Kepco power supply.

B. Magnetic field configurations

The magnetic field contour in Fig. 2 shows the MiXI thruster configured with the original 3-ring (3R),[1] a 5-ring (5R), and a 4-ring (4R) cusp configuration. The ring-cusp fields were created by an axially magnetized continuous ring magnet upstream of the chamber and radially magnetized discrete block magnets surrounding the cylindrical anode. Samarium cobalt permanent magnets were used for their

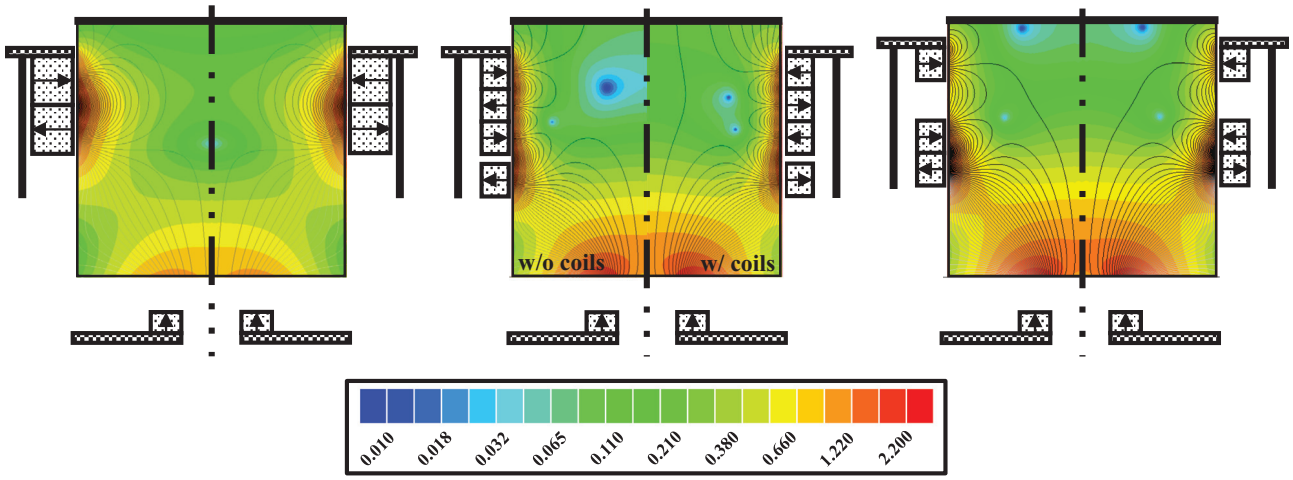

FIG. 2. Magnetic field contours in logarithmic scale (shown in kG) of the MiXI thruster test platform with the 3-ring (left), 5-ring (middle), and 4-ring (right) configurations. The computed magnetic field values are verified using a 3-axis Gaussmeter. The trims coils were placed around the thruster to allow the superimposition of an axial field inside the discharge chamber.

high field strength and operating temperatures. The B-field geometries were characterized by comparing 2D simulations to Gaussmeter measurements, shown in Fig. 4. In an earlier research effort,[17] the MiXI with a 3-ring (3R) discharge configuration was determined to have the most desirable overall performance compared to a wide range of discharge magnetic field options. The SmCo magnets used in the 3R configuration were originally used in the NSTAR thruster. As a result, these magnets only generate 70% of their original field strength at the face. This was found to provide higher efficiency and stable operation compared to a later test that used full-strength NSTAR magnets. This was because the strong field generated by the full-strength magnets led to an impedance shift instability in the discharge due to overconfinement of the plasma electrons.[17,18]

The intention of the 5R design was to maximize the low field region in the chamber to expand the effective plasma volume and improve the beam flatness.[19] The smaller magnets still produced strong cusp magnetic fields but have a shorter range compared to the 3R magnets. Preliminary simulations using a particle pusher showed a better overall primary electron confinement despite the greater total cusp leak area since the primary electrons were able to travel greater distances before encountering a cusp element where they can be lost. For some tests, trim coils were used to generate an axial magnetic field within the bulk region where the permanent magnetic fields are weaker as shown in Fig. 4.

The 4R configuration was designed based on findings from the 3R and 5R testing with the intention of improving the beam uniformity. The magnetic field shape diverges the field lines downstream from the cathode with the null region near the grid plane. The 4R design featured an isolated electrode at the downstream cusp that was biased to the cathode potential to reflect the primary electrons. This technique has been demonstrated to improve the discharge performance of larger ion thrusters by increasing the plasma density near the extraction plane.[20]

C. Simulated ion thruster performance

The ion optics for the MiXI grid system were designed for plasma densities typical of the original 3R configuration ($\sim 2 \times 10^{17}\,\mathrm{m}^{-3}$). To focus on the discharge design and reduce the design variability of the grids, the discharge was

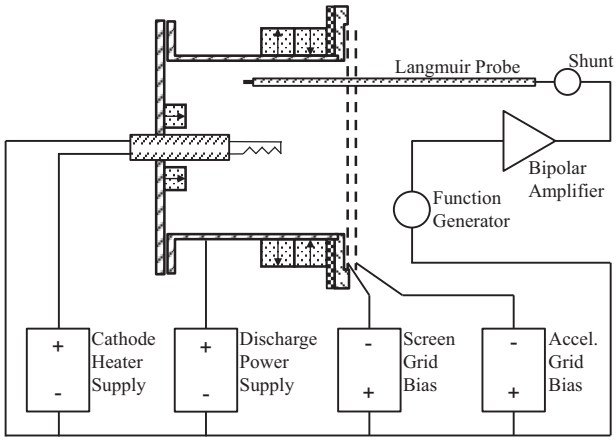

FIG. 3. The electrical diagram of the discharge test apparatus including power supplies and the Langmuir probe circuit. Since an ion beam was not produced, a beam power supply was not used and the negative terminal of the discharge supply was grounded. Reprinted with permission from Ref. 39. Authors are the copyright holder.

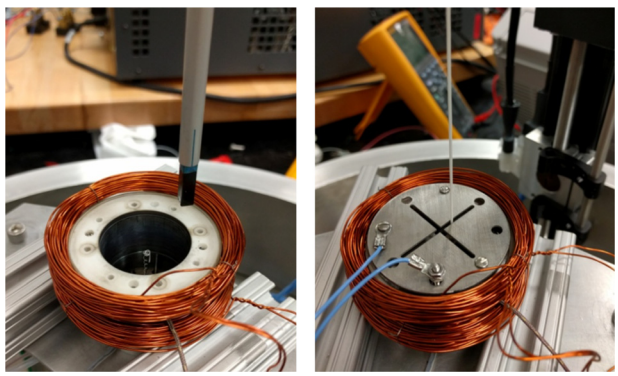

FIG. 4. Left: the MiXI thruster without the screen and accelerator grids and the Gaussmeter probe used to map the magnetic fields. Right: thruster fitted with probing grids for 2D Langmuir probe mapping of the discharge plasma. Reprinted with permission from Ref. 39. Authors are the copyright holder.

characterized without beam extraction using a simulated ion thruster or "discharge-only" operation. The predicted performance for the simulated discharge was determined using a simple model described by Brophy.[21] This methodology has previously been implemented by several researchers on different ion thrusters and has been shown to reliably predict the discharge performance.[22,23] The model accounts for an equivalent neutral flow rate since beam ions that would normally leave the thruster are instead neutralized at the grids and reinjected back into the discharge chamber as neutral particles; they thus contribute to an additional flow rate. The predicted beam current (I_b) is calculated by multiplying the measured total ion current incident to the grid system (I_g) with the reported ion transparency of the MiXI grid system, $I_b = I_g\Phi_i$. The effective neutral flow rate can then be calculated using

$$\dot{m}_p^* = \dot{m}_p + \frac{I_b}{\alpha_m}\left(\frac{M}{e}\right), \tag{1}$$

where $\dot{m}_p$ is the specified flow rate as measured by the flow controller, α_m is the doubly charged ion correction factor, and M and e are the electron mass and charge, respectively. This expression assumes that all ions collected at the accelerator and screen grids experience 3-body recombination and return to the discharge chamber as neutral atoms. Brophy determined that only ~45% of the accelerator grid ions re-enter the discharge chamber in the J–Series thruster because a fraction of the returning atoms was reflected out of the thruster by the downstream side of the screen grid. Since we assume that all potential beam ions re-enter the chamber, the performance values reported herein, are conservative with respect to this metric. The J–Series thruster has an ion and neutral transparency of 0.80% and 0.67%, respectively, compared to 0.75% and 0.05% of the MiXI thruster. Therefore, for the simulated discharge used herein, it is reasonable to assume that all of the effective beam current returns to the discharge as the neutral flux.

The expression for the discharge power must also be modified for the electrical configuration shown in Fig. 3. The beam ions in a flight thruster are neutralized by a cathode external of the discharge chamber. These electrons have negligible power consumption due to the low coupling voltage to the neutralizer cathode. In a simulated ion thruster, these ions are lost to the grids and the electrical current is instead balance with the discharge electrons that are extracted at the discharge voltage. Therefore, the beam current must be subtracted from the discharge current when calculating the discharge power and the expression for the discharge loss is written as

$$\epsilon_b = \frac{(I_d - I_b)V_d}{I_b}, \tag{2}$$

where I_d and V_d are the discharge current and power, respectively. The mass utilization efficiency (η_{ud}), electrical efficiency (η_e), and total efficiency (η_T) are calculated using the same standardized expressions.

The beam flatness parameter is generally calculated from the ion beam current-density profile, measured directly downstream of the accelerator grid. To predict the beam profile and flatness parameter in the simulated ion thruster, the ion current-density is instead extrapolated from the internal plasma parameter maps that will be presented in Sec. III B. The extraction for each individual beamlet is approximated as a flat planar sheath and the ion beam current-density can be described by multiplying the Bohm ion current[24] with the ion transparency

$$j_B^*(r) = 0.6en_i(r)\sqrt{\frac{kT_e(r)}{m_i}}\Phi_i, \tag{3}$$

where the ion density (n_i) and electron temperature (T_e) are taken from the discharge map along the screen grid plane.

The discharge performance data were measured by keeping the discharge voltage constant and slowly increasing the discharge current by adjusting the cathode filament heater power. Performance data were acquired at discrete flow rates and trim coil settings. The performance results were calculated with assumptions based on the operational data of the original MiXI thruster with beam extraction, shown in Table I. This includes: 1100 V beam voltage, grids with 75% ion transparency, no beam divergence, and a negligible doubly charged ion population. The beam divergence in the MiXI thruster was calculated to be ~5° based on Faraday probe measurements of the ion beam—this translates to a less than 1% reduction in the total efficiency. The high neutral density of the MIXI thruster (afforded by the SHAG optics), low electron temperature, and low ionization percentage leads to negligible doubly-to-singly charged ion ratios.[15] In addition, the performance figures shown in Sec. III will not include possible additional power usage and/or gas flow for the discharge and neutralizer cathode. The total efficiency to be presented in Fig. 6(b) only serves the purpose as a comparison metric between the simulated and beam extracted performance of the 3R configuration and between the various configurations discussed in this paper.

D. Discharge mapping

A set of 0.75 mm thick stainless steel probing grids was fabricated and installed in lieu of the original MiXI grids, as shown in Fig. 4. The probing grids feature a 1.5 mm thin slit across the chamber diameter for full probe access. The

TABLE I. Performance data for the 3-ring MiXI thruster calculated from the total extracted ion beam and beam profile.[25]

Parameter	Values
Beam voltage	1089 V
Beam current	28.3 mA
Discharge voltage	25 V
Discharge current	0.503 A
Flow rate	0.51 sccm
Discharge loss	444 eV/ion
Propellant efficiency	0.79
Total efficiency	0.56

additional perpendicular slit was originally designed to match the total open area of the MiXI grids but later proved unnecessary due to the cutting resolution of the water-jet. To account for the increase neutral transparency, the gas flow rate was increased by a factor of 2.5 times to match the discharge conditions when operated using the MiXI grids. The set of probing grids were spaced roughly 3 mm apart to minimize the escape of charged particles. The Langmuir probe was able to access an entire azimuthal slice of the discharge chamber sans the region very near the cathode filament.

Figure 5 is a diagram of the 3R configuration overlaid with a typical raster scan pattern used in the discharge maps. Each scan generally includes over 500 data points with smaller step sizes near the cusp for higher resolution in the high B-field regions of the discharge. The plasma properties were measured using a cylindrical Langmuir probe, constructed with a 1.2 mm length by 0.2 mm diameter tungsten wire protruding from a 1.1 mm diameter alumina tube. The preliminary tests were used to confirm that the Langmuir probe does not significantly disturb the discharge plasma during operation. There is at most a 2% effect on the discharge current and estimated beam current when the probe was scanning near the center-line upstream region inside the discharge chamber.

The Langmuir probe measurements were analyzed using the standard probe theory for the plasma potential and electron temperature. The electron retarding region of the standard current-voltage *I–V* curve, particularly near the plasma potential, can be strongly affected by the local magnetic field. The plasma potential was found at the maximum first derivative of the *I–V* data. The second derivative data was used to calculate the electron temperature using a Maxwellian fit in the region near the floating point potential. This method distinguishes between the primary and plasma electron population and avoids fitting near the plasma potential as the low energy electrons are more affected by the magnetic fields. The plasma density was calculated from the ion saturation curves that are less affected by the magnetic fields. The Bernstein-Rabinowitz-Laframboise (BRL)[26] theory was employed for the ion fit using the parametrized curves generated by Chen.[27] The theory accounts for the effects of sheath expansion and ion orbital motion for small diameter probes.

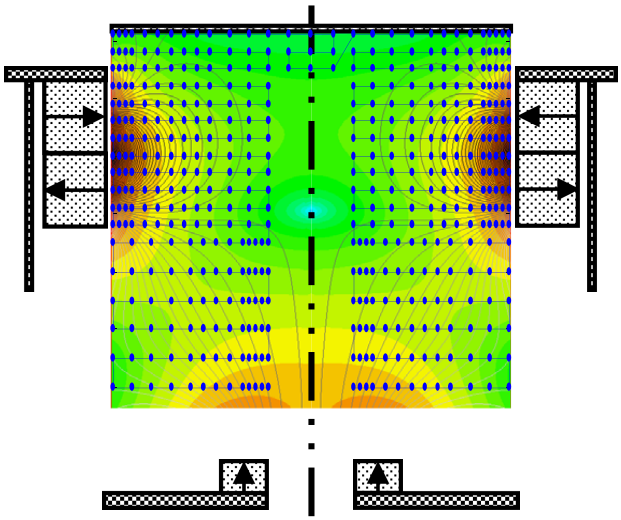

FIG. 5. Example Langmuir probe scan pattern used to generate the discharge maps overlaid onto the magnetic field contour. The center region is empty to avoid contact with the discharge filament.

The magnetic fields affect the collection of electrons to the probe; the magnitude of which depends on the magnetic field strength and orientation relative the probe, the probe size, and the energy distribution of the electrons. Very near the cusps (~2000 G), the magnetic field affects both the primary and plasma electrons. Toward the vicinity of the bulk plasma (~250 G for the 3R discharge), the gyro-radius of a 1 eV electron is already greater than the radius of the Langmuir probe and the magnetic field has a lesser effect on electron collection. There are more complicated Langmuir probe theories for magnetized electron collection that may yield a more accurate plasma potential.[28–30] However, they are prohibitively difficult to implement in the mapping of a ring-cusp discharge since the magnetic field strength and orientation vary significantly throughout the chamber. In addition, the errors associated with the probe analysis are systematic and the results are sufficient for a qualitative comparison between the various discharge conditions.

Druyvesteyn showed that the electron energy distribution function can be extracted from the second derivative of the *I–V* characteristics[31]

$$F_e(\varepsilon) = \frac{2}{A_p e^2}\sqrt{\frac{2m\varepsilon}{e}}\frac{d^2 I_e}{dV^2}, \tag{4}$$

where A_p is the total area of the probe and ε is the electron energy (eV) which corresponds to the probe's voltage with respect to the plasma potential (i.e., $\varepsilon = V_p - V_{lp}$). The electron density can then be calculated by integrating $F_e(\varepsilon)$ across the entire energy spectrum

$$n = \int_0^\infty F(\varepsilon)d\varepsilon. \tag{5}$$

The primary electron energy distribution is found by subtracting the fitted Maxwellian curve for the plasma electron population from the second derivative data. The approximate primary electron density can then be calculated by integrating the remaining energy distribution. The local average primary electron energy is calculated from

$$\bar{\varepsilon} = \int_0^\infty F(\varepsilon)\varepsilon d\varepsilon \Big/ \int_0^\infty F(\varepsilon)d\varepsilon. \tag{6}$$

E. Ion generation and primary electron loss rates

The ion generation rates and primary electron loss behavior throughout the discharge chamber can be calculated from the plasma parameter maps. The generation rates of singly (I_R^i) and doubly charged (I_R^{ii}) ions are estimated through probabilistic collision calculations using differential collision cross-sections[32–34] for the corresponding interactions

$$I_R^i = n_0 n_e \langle \sigma_i v_e \rangle \forall + n_0 n_p \langle \sigma_i v_p \rangle \forall, \tag{7}$$

$$I_R^{ii} = n_i n_e \langle \sigma_{ii} v_e \rangle \forbidden + n_i n_p \langle \sigma_{ii} v_p \rangle \forbidden, \tag{8}$$

where n_0, n_e, n_i, and n_p are the neutral, plasma electron, ion, and primary electron densities, receptively. $\forbidden$ is the volume, v is the velocity of the incident particle, and σ is the collision cross-section of the interacting particles. The angle bracketed terms represent the reaction rate coefficients that can also be expressed as the particle's velocity multiplied by the reaction's collision cross-section. The reaction rates for plasma electrons are calculated by integrating over the Maxwellian distribution for a given plasma electron temperature. The voltage across the filament heater leads to a large energy spread for the primary electrons; therefore, their reaction rate coefficients were calculated by integrating the primary EEDF determined from the probe data

$$n_p \langle \sigma_i v_p \rangle = \sqrt{\frac{2}{m}} \int_0^\infty F_p(\varepsilon) \sigma(\varepsilon) \sqrt{\varepsilon} d\varepsilon, \tag{9}$$

where $\sigma(\varepsilon)$ is the differential cross-section and $F_p(\varepsilon)$ is the primary EEDF. For all discharge conditions presented in this paper, there was a negative-going sheath to all surfaces within the chamber walls. Therefore, the ion wall loss can be estimated by integrating the Bohm current at the edge of the discharge map. The remaining ion loss to the filament, filament holder, and upstream cathode surface near the centerline was estimated through a current balance between the total ion production and loss to other surfaces.

In addition to the primary electron loss to ionization, they are also lost to the chamber walls, excitation collisions, and thermalization. The excitation loss is calculated in an identical manner to ionization using the corresponding cross-sections. The reaction rate for thermalization is calculated using the Spitzer[35] slowing down time (τ_s), where $n_0 \langle \sigma_s v_p \rangle = \tau_s^{-1}$. The primary electron wall loss cannot be reliably calculated in the same manner as the ions. The magnetic fields and the negative-going sheath reflect an unquantifiable portion of the primary electron population incident to the walls. However, the primary electron power wall loss (P_w) can be estimated using a power balance with the discharge power (P_d) by integrating over the primary EEDF

$$P_d = \int_{\forbidden} (R_i E_i + R_{ii} E_{ii} + R_{ex} E_{ex} + P'_{pl}) d\forbidden + P_w, \tag{10}$$

where R_* is the local reaction rate, $R_* = I_R^* / \forbidden$, E_* is the energy required for each corresponding interaction,[32,33] and the subscripts "ex" represents the excitation collisions. P'_{pl} is the primary electron power per volume deposited into the plasma electron population which can be estimated by

$$P'_{pl} = R_i (E_p - E_i) + R_{ii} (E_p - E_{ii}) + R_{ex} (E_p - E_{ex}) + \frac{n_p}{\tau_s} \bar{\epsilon}_p, \tag{11}$$

where $\bar{\epsilon}_p$ is the average primary electron energy calculated from the local EEDF data. In this calculation, it is assumed that all remaining primary electron energy after an inelastic collision is transferred to the plasma electrons. The Spitzer slowing rate is much higher for these slower energetic electrons while their confinement time is longer. However, the error associated with this assumption will depend on the lossiness of the discharge design.

F. Operating conditions

The performance and discharge mapping data were all acquired with the same relevant discharge operating conditions. The screen and accelerator grids were biased to 5 and 20 volts below the cathode potential, respectively. An additional collector plate downstream of the thruster confirmed that there was negligible ion current leaving the discharge. The discharge voltage was kept at 25 V for all tested conditions, despite certain field configurations showing better performance at lower or higher voltages. The discharge voltage in most modern ion thrusters is usually limited to under ~25 V to prevent excessive erosion of the discharge hollow cathode and screen grids; the xenon-incident sputtering threshold energy for molybdenum is 27 V, measured experimentally.[36] The discharge current is controlled by adjusting the filament cathode heater power. Measurements were acquired once the discharge performance stabilizes when thermal equilibrium was reached.

III. RESULTS AND DISCUSSION

This section compares the 3R, 5R, and 4R configurations via discharge performance and simulated thruster performance metrics. These performance trends are used to assess the macroscopic discharge plasma behaviors. The results of the discharge plasma parameter are then used to estimate the species reaction rates within the discharge and to understand the overall performance behavior.

A. Performance data analysis

The performance curves at different specified flow rates are shown in Fig. 6. Although it appears as if the discharge performs universally better at higher flow rates, the beam current is not constant along each curve, unlike standard performance plots. Figure 6(b) expectedly shows that the discharge is more efficient at lower flow rates when extracting lower beam currents and vice versa.

Despite the simulated ion thruster operation, estimates of the thruster efficiency and discharge characteristics were similar to those previously obtained by Wirz with beam extraction, summarized in Table I. Inspection of the 0.140 sccm flow rate at the 25 V, ~0.50 A discharge condition shows that the beam current, discharge loss, and total efficiency values are within 5% of those obtained with beam extraction. The slight differences are possibly caused by the cathode filament placement and extraction characteristics of the grids. The close agreement provides confidence of using the simulated discharge operation to obtain accurate performance values for other magnetic field configurations and discharge conditions.

Figure 7 is a performance comparison between the 3R, 4R, and 5R magnetic field configurations. The performance curves shown for each configuration represent the specified flow rate that exhibited the highest total efficiency at ~30 mA of beam current for the available data. The results show that the 3R outperforms the non-trimmed 5R configuration. The

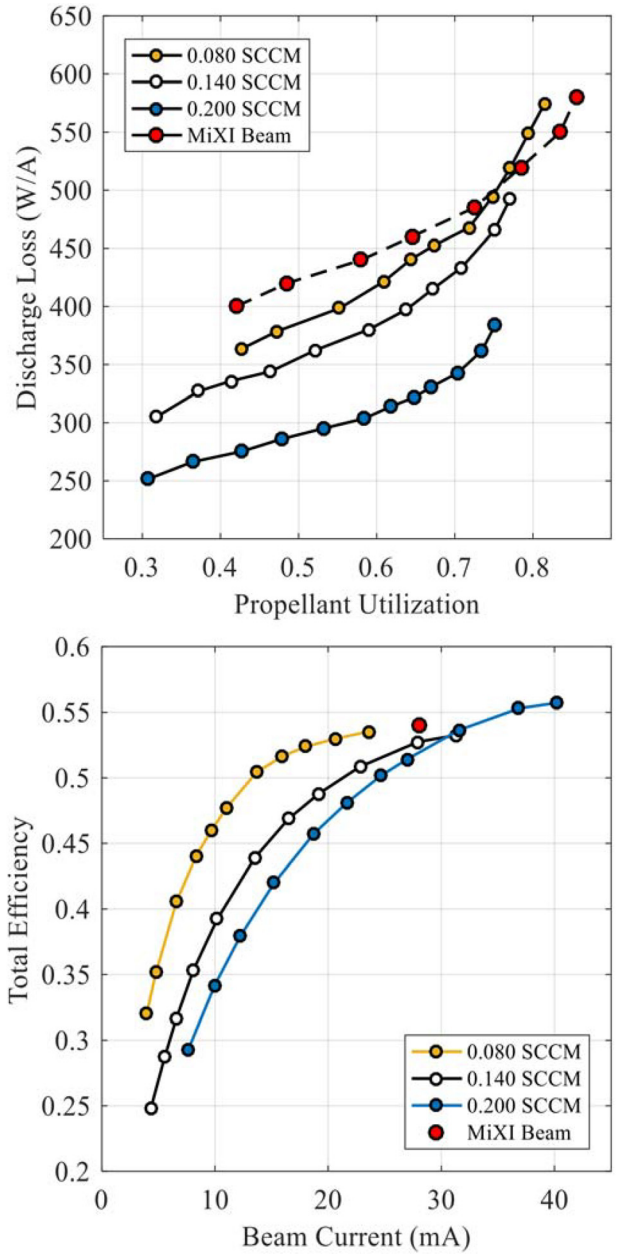

FIG. 6. Performance assessment of the 3R configuration at a range of base neutral gas flow rates. The curves are generated by adjusting the heater power to increase the discharge current while keeping all other supplies constant. The red-filled circle represents the performance of the MiXI thruster with beam extraction.

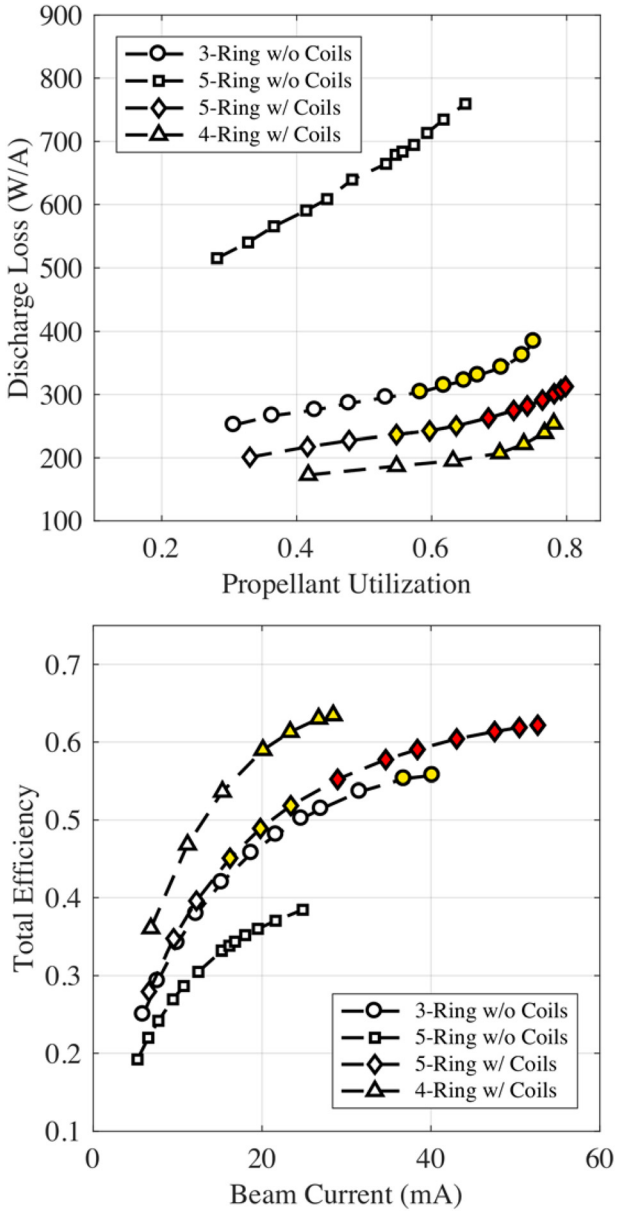

FIG. 7. Performance comparison of the 3R, 5R, and 4R configurations. The yellow and red marker fills indicate a peak beam current density higher than the optimal and perveance limit of the MiXI ion optics, respectively.

non-trimmed 5R performance was similar to the 3R configuration near the start of testing and gradually decreased as thermal equilibrium was reached at higher discharge powers. This performance loss was caused by demagnetization of the permanent magnets (up to 40% reduction at the magnet face) due to excessive temperatures and was confirmed with Gaussmeter measurements. The performance of the partially demagnetized 5R configuration increased gradually with increasing trim coil currents, reaching a maximum with an additional ~60 Gauss of the trim B-field. The trim coils allow the 5R performance to exceed the 3R configuration by a notable margin, achieving higher propellant utilization and lower discharge loss at a given beam current. However, these performance values do not affect important parameters such as beam flatness. The yellow marker fills indicate the discharge condition in which the peak beam current density surpasses the acceptable lifetime conditions for the MiXI grid system at ~6 mA/cm^2. The red marker fill data points indicate a peak beam density that surpasses the perveance limit of the grids. Exceeding the perveance limit leads to direct impingement of high energy beam ions on the accel grid and rapid accel grid erosion. The peak beam density is calculated through scaling of the simulated beam profile from the discharge map shown in Fig. 12.

Performance data with respect the various discharge voltages and base flow rates were not obtained for the 5R configuration. It was noted that the discharge loss did decrease with increasing discharge voltage, unlike the 3R configuration where the opposite trend was measured. The performance plot for the 4R configuration, shown in Fig. 8, was obtained

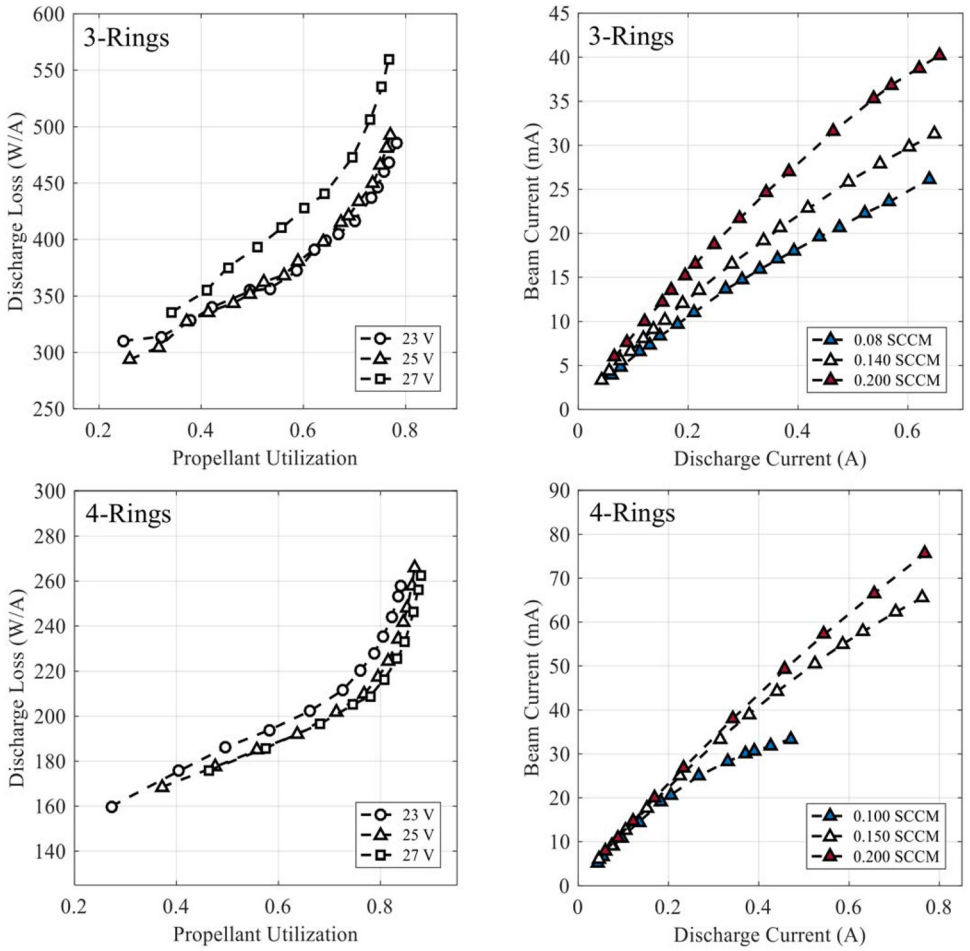

FIG. 8. Comparison of the simulated ion thruster performance data between the 3-ring (3R) and 4-ring (4R) configuration. The results show opposing trends between the discharge design with good and poor primary electron confinement.

after analyzing the first discharge mapping data for the 3R and 5R configuration. The performance and efficiency measurements, shown in Fig. 7, were very promising but as previously mentioned, the discharge mapping data for this configuration will show a structure that is incompatible with ion thrusters. However, the confinement mechanism is similar to the 5R configuration and the more extensive performance data set acquired is useful for the purpose of discussion.

Focusing on the comparison of the discharge performance curves between the various discharge voltages in Fig. 8 shows an uncommon trend in the 3R configuration. Generally, raising the discharge voltage directly increases the primary electron energy and ionization rate which would typically result in a lower discharge loss. This trend is ambiguous with in the 3R performance data, and in some cases, the opposite trend is observed. The behavior is a result of the poor primary electron confinement of the 3R discharge as most of the primary electrons are lost to the walls before colliding with a neutral atom. Therefore, most of the added discharge energy has a small effect on ionization and instead contributes to an additional electrical loss. On the other hand, the 4R configuration exhibits a good primary electron confinement and the discharge is more electrically efficient when operated at a higher discharge voltage.

This analysis is also supported by inspecting the beam current in relation to the discharge current for the different specified flow rates in Fig. 8. The ionization path length is inversely proportional to the neutral density, while the primary confinement stays relatively constant. Since there is no beam extraction, the dominant mechanism of xenon particles escaping from the discharge chamber is thermal motion through the gridlets. Most of the neutral gas heating is indirectly through radiation from the filament cathode and the chamber temperature remains relatively constant throughout the discharge current sweep. Therefore, each specified flow rate curve corresponds to a constant neutral density inside the chamber despite the changing discharge conditions. The results show that for any given discharge current, the 3R beam current increases with the neutral gas density. As the ionization path length decreases, a greater ratio of primary electrons is able to encounter an inelastic collision before being lost to the walls.

The same plot for the 4R discharge exhibits a slightly different trend, where increasing the neutral gas density does not noticeably increase the beam current below 0.2 A of discharge current. This indicates that almost none of the primary electrons are lost to the walls at the lowest tested neutral density. The plasma generation is only limited by the available discharge energy and increasing the flow rate only reduces the propellant efficiency. At discharge currents greater than 0.2 A, the data shows that the beam current plateaus off quicker at lower specified flow rates because of the

neutral gas depletion. The higher ionization ratio of the plasma and higher electron temperatures increases the loss mechanism for all charged species.

The assumption of a constant 75% ion transparency is the largest source of uncertainty with the simulated performance results. Ion thruster grids are generally designed for a specific plasma density across the extraction plane in order to ensure desired focusing of the beamlets through the accelerator grid. Although the bulk plasma density can be adjusted with the discharge power, the ion transparency is a function of the upstream plasma properties and significant variations, most notably the plasma density, along the extraction plane would overestimate the performance. The operating temperature was noted to affect the performance results by increasing the rate of neutrals escaping the grids. Although measurements were acquired at similar temperatures for each configuration, operating at thermal equilibrium can reduce the total efficiency by up to 4% compared to normal operating temperatures of conventional ion thrusters ($\sim 150 - 250\,^{\circ}\mathrm{C}$). Measurement errors for the performance results are negligible compared to the previously mentioned uncertainties. The flow controller has a 0.2% accuracy from a full scale of 1 sccm. The errors associated with the instrument accuracy and noise results in less than a 1% uncertainty to the data.

B. Discharge map analysis

The four plots shown in Fig. 9 are sample Langmuir probe data and analysis at an arbitrary location inside the 3R discharge. The top right plot shows the standard *I–V* trace in a semi-log plot along with the calculated first and second derivative. From visual inspection, the standard *I–V* sweep would yield a slightly higher electron temperature than that from the derivative curves because of the primary electrons. The primary electron population can be resolved and detected in the second derivative data by the kink in the curve at the higher energies. The bottom left figure shows the process of calculating the primary electron density. They are defined here as the difference between the full population and Maxwellian estimate for the plasma electron population. The bottom right plot shows the ion saturation fit using the BRL theory which iterates to a plasma density based on the sheath size.

The results, shown in Fig. 10, are interpolated contour plots of the plasma parameters for the 3R configuration measured at 0.35 A discharge current and 0.140 sccm specified flow rate. The plasma density structure shows a strong correlation with the magnetic field structure shown in Fig. 2, an attribute resembling the results found by Mao and Wirz.[14] The primary electron contour coincides within the plasma density structure and the population accounts for more than $\sim$10% of the total electron density within the bulk plasma. The electron temperature ranges between 2.5 to 3.0 eV and exhibits a more gradual delineation compared to the density contours. The plasma potential is by and large uniform at $\sim$28 V relative to the cathode potential within the entire discharge chamber.

The 3R configuration shows a remarkably flat projected beam profile similar to the extracted beam measurements previously reported by Wirz. Figures 2 and 10 reveal that the

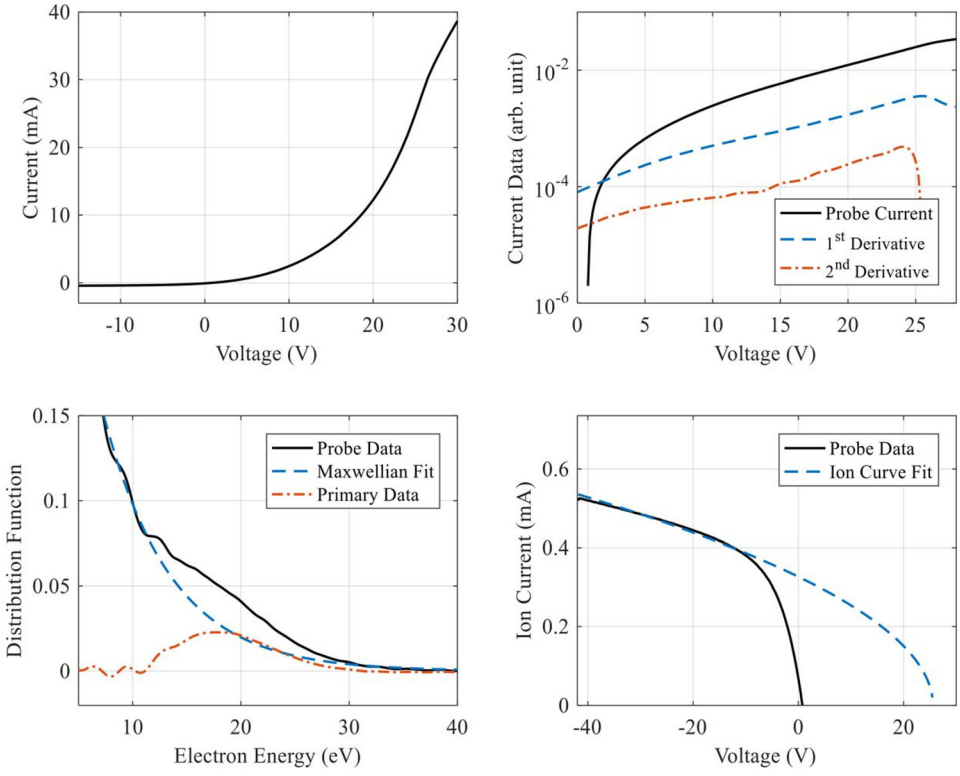

FIG. 9. Example Langmuir probe data and analysis. (a) The binned and then averaged I-V sweep. (b) The probe sweep and its derivative plotted in a semi–log scale. (c) Extraction of the primary electron density through subtraction of a Maxwellian plasma electron population. (d) The ion saturation curve fitted using the BRL method.

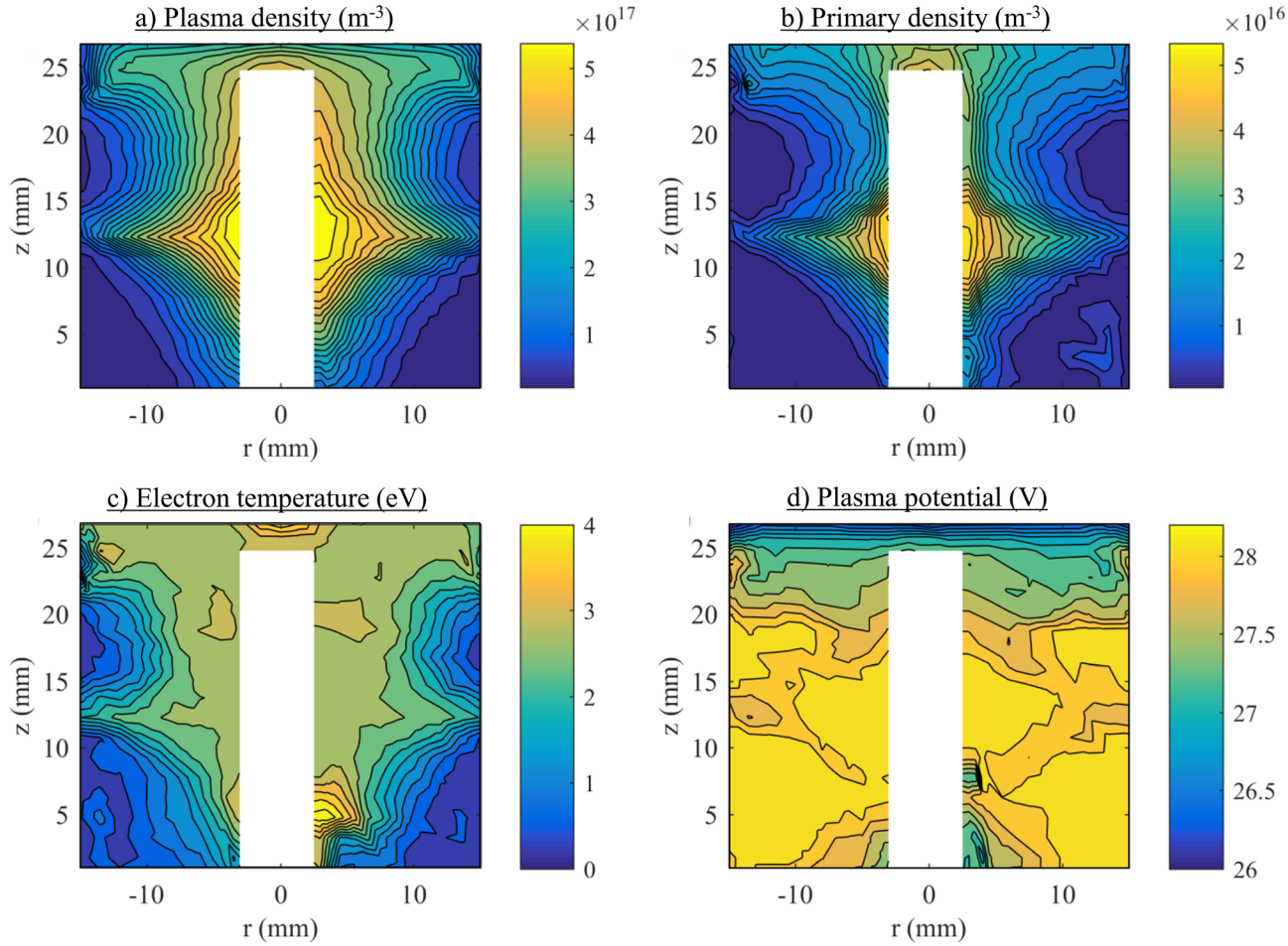

FIG. 10. Discharge mapping results for the 3R configuration showing the: (a) plasma density (m^{-3}), (b) primary electron density (m^{-3}), (c) electron temperature (eV), and (d) plasma potential (V). The cathode filament is located in the empty rectangular space at the center that is not probed. Reprinted with permission from Ref. 39. Authors are the copyright holder.

MiXI discharge field topology aligns the cusp and plasma structure across the extraction plane. This topology is produced by the two closely spaced ring-cusps which push the null region of the downstream ring-cusp past the grid plane. Therefore, the primary electrons are confined in between by the magnetic cusp and the grids at the cathode potential. This feature produces a high beam flatness parameter despite the strong radial B-field gradient. However, the two ring-cusps also produce a relatively strong virtual point-cusp in between the two null regions. The plasma and primary electron densities are shown to peak at the upstream ring-cusp null region—hence, they are partially confined by the virtual point-cusp from freely diffusing to the screen grid region, leading to high wall losses in the upstream region.

The overall low electron temperature is an indication of poor primary electron confinement as most of the discharge energy was lost directly to the chamber walls rather than to ionization or thermalization. As a consequence, the majority of the ionization is directly from primary electron bombardment rather than the high energy tail of the plasma electron population. The primary electron densities are higher than conventional-size discharges and their structure resembles a skeleton of the plasma density contour. In addition, the plasma potential values indicate a strong negative (electron-repelling) sheath of about one electron temperature to the anode. The sheath potential is self-consistently established in order to maintain charge quasi-neutrality within the plasma. The high sheath potential indicates an excessive anode area due to poor magnetic confinement of the electrons. The negative sheath is a poor mechanism for electron confinement because the electrostatic field essentially reflects only the low energy electrons and the ionizing electrons are disproportionally lost.

The contour plots in Fig. 11 are a comparison of the plasma parameters for the 5R configuration, measured at the same discharge and flow conditions, with and without the trim B-field. The discharge plasma without trim coils exhibits characteristics similar to the 3R configuration but with poorer confinement. The plasma density, primary density, and electron temperature are lower throughout the discharge. The bulk plasma extends almost entirely to the chamber walls due to the larger low B-field region and weaker cusp fields. With the addition of the trim coil fields, there is a large increase in plasma density, primary density, and electron temperature. As shown in Fig. 2, the trim coils generate a predominately axial magnetic field in the bulk plasma which obscures any direct path of the primaries to the anode wall. Therefore, the primary electrons are confined to the center-line of the discharge where the primary density is over 4 times greater than without the trim fields. Subsequently, the electron temperature is almost twice as

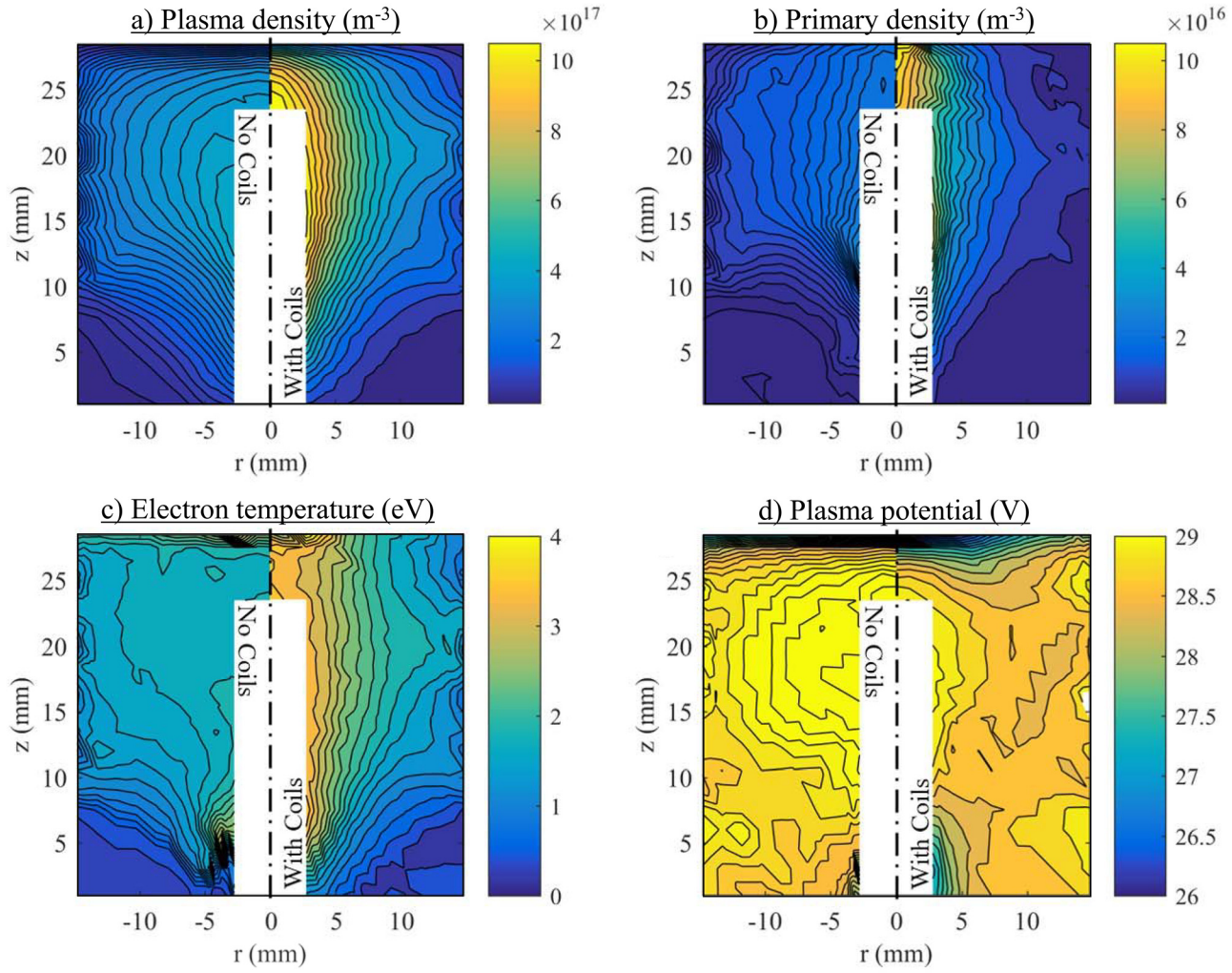

FIG. 11. Discharge mapping results of the modified 5R configuration with the same units as Fig. 10. The left and right side of each contour map show the plasma structure with and without the trim coil magnetic fields. Reprinted with permission from Ref. 39. Authors are the copyright holder.

high within the center-line region and higher throughout the discharge chamber. The more pronounced gradient along the radial direction is expected as electrons must now diffuse across axial magnetic fields to reach the anode. The higher center-line primary density and electron temperature lead to a local increase of the ionization rate and plasma density values that are up to 2.5 times greater than the non-trimmed condition. The plasma potential, although lower than the non-trimmed result, is still almost an electron temperature above the discharge voltage and indicates that there are still high plasma electron losses to the chamber wall.

The strong center-line densities are traits similar to earlier Kaufman ion thruster designs, which are an adaptation of Penning ion sources, which also use a predominately axial magnetic field. Oscillations were detected in the Langmuir probe measurements for the 5R w/coil condition. The oscillation frequency ranged from 1 kHz to 20 kHz and increased monotonically with the trim coil field strength. However, the discharge current did not exhibit oscillations, which suggests that these probe oscillations are likely azimuthal. This is also similar to some Kaufmann thrusters, where $E \times B$ driven instabilities have been shown to facilitate the radial transport of electrons.

The results show that the performance leap in the 5R trimmed configuration is almost entirely attributed to the improved confinement of the primary electrons. Comparing the primary electron density contours between the 3R and 5R configuration shows a large difference between the losses to the anode wall. The primary electron's elastic collisional cross-sections are similar to the ionization cross-sections. Therefore, they do not encounter many scattering collisions that would allow them to diffuse across the magnetic field lines before they are lost to ionization or thermalization. Most of the plasma electron population, on the other hand, does not have sufficient energy for ionization or excitation. The collisional plasma electron population can more easily diffuse across the magnetic field lines. In the standard ring-cusp ion thruster design, the fields of each individual ring-cusp diverge directly into the bulk plasma. Consequently, the plasma and primary electrons losses are coupled together, leading to a high primary loss at the smaller-scale. The weak axial fields in the 5R discharge establish a "magnetic filter" in front of the cusp element to prevent primary electron loss without strongly impeding the collection of the discharge current.

Figure 12 shows the projected normalized beam profile for each configuration, calculated from the plasma density

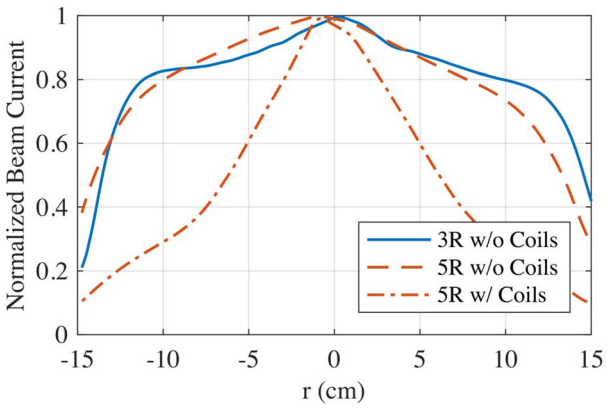

FIG. 12. Normalized beam current for each configuration, estimated from the plasma conditions measured near the exit plane of the discharge. Note: the beam current estimates are based on an ion transparency of 75%, assumed across the grid plane and grid perveance considerations are not included.

and electron temperature values along the extraction plane. Although the 5R trimmed theoretical operated more efficiently, as measured by the greater total ion current collected at the grids, the beam profiles show that it also has the poorest beam flatness. With the MiXI grids, the 5R trimmed performance is appreciably overstated as the beamlet current surpasses the perveance limit of the grid design. In addition, the highly non-uniform beam would lead to faster and uneven erosion of the extraction grids or design difficulties to account for the steep density gradient. In addition, the high center-line primary density may lead to a high local generation of doubly charged ions. The NSTAR thruster also exhibited a similar behavior of axially confined primary electrons (albeit less severe), which was found to deplete the neutral population and increase the local ionization fraction.

The main sources of uncertainty in the discharge mapping results are the accuracy and implementation of the various Langmuir probe theories. As previously discussed in Sec. II D, there is a wide range of plasma conditions and magnetic field properties inside the discharge chamber that affect the accuracy of the analysis. The standard deviations of the *I–V* trace shown in Fig. 9 were ∼20% of the mean values for the entire range of the sweep. The measurement resolution was kept constant throughout the mapping process and thus, there is low precision of the measurements at the very edge of the bulk plasma. Nonetheless, the primary intent of the discharge maps is to provide qualitative insights into the relative plasma structure and behavior between the discharge configurations investigated herein.

C. Ion and primary electron rate analysis

The singly and doubly charged ion generation rate contour maps for the 3R and 5R coiled configuration are shown side-by-side in Fig. 13. The primary electron excitation and thermalization contour maps are shown in Fig. 14. The contour map for the untrimmed 5R configuration is qualitatively similar to the 3R analysis and is not presented here. The volume averaged rates are tabulated in Table II but have high expected errors because of the following factors. First, the plasma density at the extraction plane is expected to be lower than when operated with a proper grid system due to the high local neutral transparency. Second, the local depletion of the neutral density in the bulk plasma generation region and overall gradient in the axial direction is not accounted for. Lastly, the plasma parameters in the filament region must be interpolated as well as charged particles loss to the cathode filament. Nonetheless, the following results and the volume-averaged analyses are useful for comparison of the behavior for the different confinement approaches.

For the 3R configuration, the results are consistent with a very weakly ionized, low electron temperature plasma. The low plasma-to-neutral density ratio and high wall loss result in a very low transfer of energy between the primary and plasma electron populations. This is evident in the low thermalization rates shown in Fig. 14(b) and quantified in Table III, which leads to the overall low electron temperature. The low plasma density also means that there are negligible double ion generation rates (<1%) since electrons are much more likely to collide with a neutral atom than an ion. As previously surmised, most of the ions are generated directly from primary electrons. Figure 13 and Table II support previous findings by Wirz that the MiXI discharge is a "primary ionizing," which accounts for over 80% of the total generated ions. Also shown in Table II, there is estimated to be a high ion loss to the filament and the upstream cathode surfaces. As discussed in Sec. III B, the peak ion density is at the upstream null region. It is suspected that a large portion of the ions generated in this region is collected by the filament and filament holder. These components reside along the virtual point cusp, in which the ions must diffuse to reach the extraction plane. Table III also supports the simulated performance data analysis in Sec. III A, which indicated that a majority of the primary electron energy is deposited directly on the anode walls. Lastly, the excitation rates are similar to the ionization rates since their cross-sections are similar and the interacting particles the same.

The 5R coiled contours show that there is elevated ion generation along the centerline region. The axially confined primary electrons lead to locally increased thermalization rates, plasma density, electron temperature, and ionization rates from plasma electrons. In contrast, the total volume generation is estimated to be similar to the 3R discharge because the centerline region accounts for only a small portion of the total volume. Table II indicates that there is higher ion loss to the cylindrical walls compared to the 3R configuration. The weak axial magnetic fields of ∼60–100 G are adequate for primary electron confinement, but are insufficient to confine the diffusive plasma electrons with a hybrid Larmor radius on par with the radius of the discharge chamber. There is still high ion loss to the filament due to the axial generation but much lower than the 3R discharge as the plasma is not confined to the centerline because of the weak B-fields. Although the doubly charged ion generation rate is slightly higher than the 3R discharge, the localized and volume rates are still negligible. The plasma mapping data alone are insufficient to estimate the double ion generation, particularly when it is caused by localized neutral depletion. An additional neutral model is required estimate the neutral

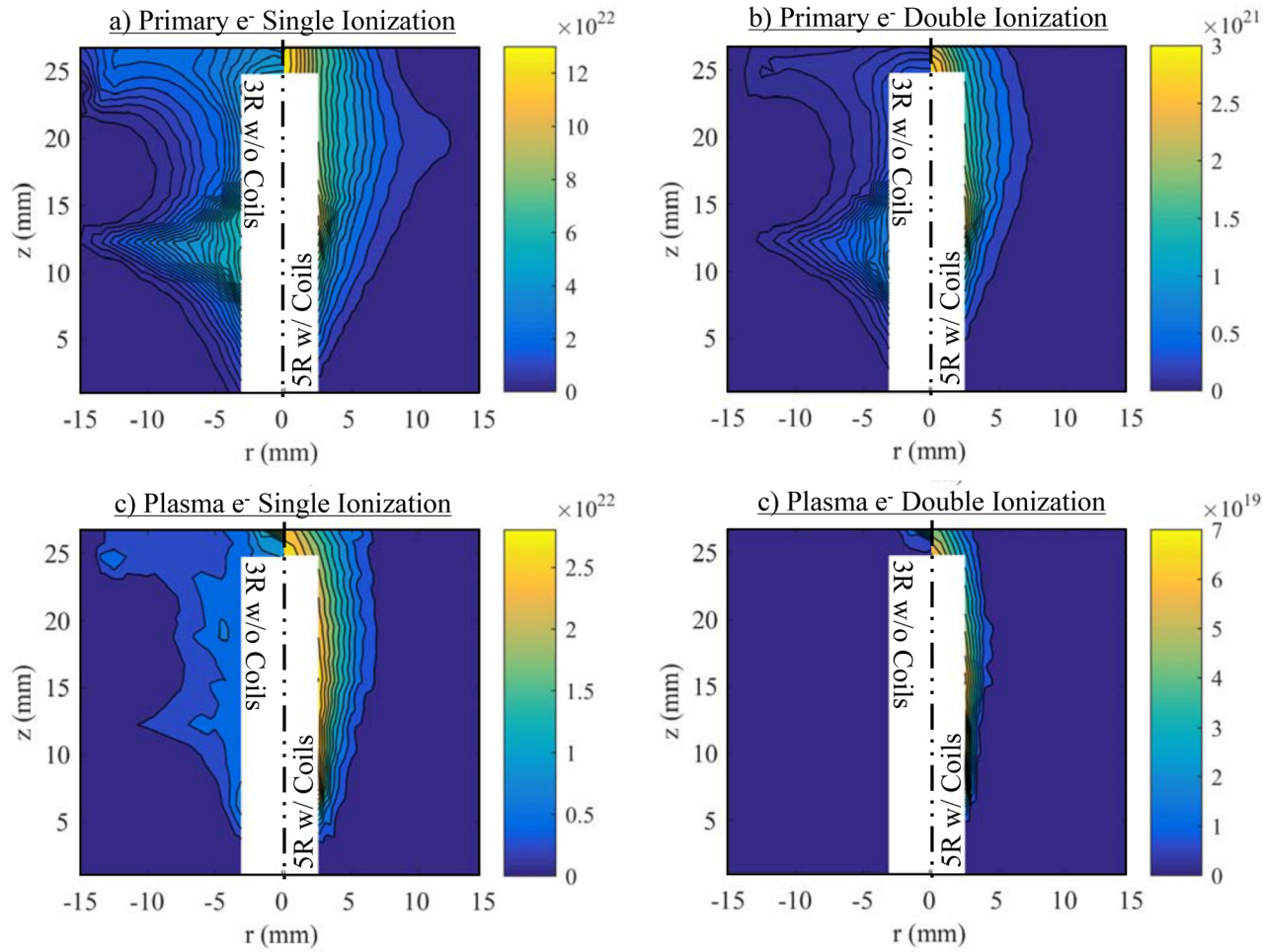

FIG. 13. Contour maps of the local reaction rates (A/m^2s) for singly and doubly charge ion generation through ionization collision by primary and plasma electrons. The left and right side of each map represent the 3R and 5R trimmed configuration, respectively.

density distribution rather than using a volume-averaged value based on the total flow rate and grid transparency.

Table III seems to suggest that there is still high primary electron loss to the walls for the 5R trimmed condition despite Fig. 11 showing low primary density along the anode walls. It is suspected that the primary electrons are being collected by the ceramic filament holder and the cathode surface upstream. Despite the 25 V discharge and the plasma potential of ~28 V at the filament, the sample EEDF shown in Fig. 9(c) seems to indicate the presence primary electrons with energies greater than what could be obtained by electrostatic acceleration through the filament sheath. This

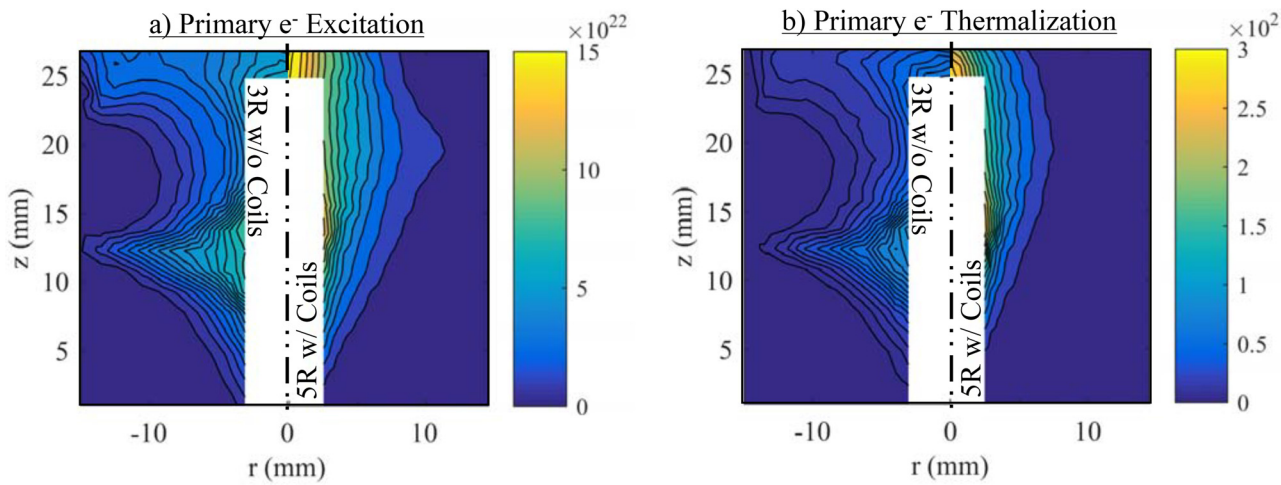

FIG. 14. Contour maps of the local reaction or loss rates for the primary electrons through excitation and thermalization. The primary electron loss rates for ionization collisions are identical to the ion generation rates in Fig. 13.

TABLE II. Ion generation (P) and loss (L) rates (mA) for the various discharge configurations. The generation terms are calculated from volume integration of the generation rates and the loss terms from surface integration using the plasma parameter maps.

Configuration	P_p^+	P_e^+	P_p^{++}	P_e^{++}	P_{total}	L_{Grid}	L_{Side}	L_{Rear}	$L_{Cath.}$
3R w/o coils	68.9	10.4	0.45	~0	79.7	22.6	9.4	1.3	46.5
5R w/o coils	37.5	0.14	0.20	~0	37.8	17.0	18.9	1.00	1.90
5R w/coils	66.2	12.5	0.9	~0	79.6	26.4	25.8	1.2	22.4

TABLE III. Breakdown of the estimated primary electron power loss mechanisms. The Spitzer term (P_{spz}) is also included into the power loss to thermalization (P_{th}).

Configuration	P_d (W)	P_{ion} (%)	P_{ex} (%)	$P_{th}(P_{spz})$	P_{wall} (%)
3R w/o coils	6	14	14	27% (7%)	45
5R w/o coils	6	8	8	16% (4%)	67
5R w/coils	6	14	13	27% (11%)	46

anomalously high energy primary population, which is outside the error of the analysis, would be able to overcome the negative-going sheath at the upstream cathode surface. Although unsubstantiated in this experiment, it has been shown that a bump-on-tail two-stream instability can lead to a phase-space oscillation of the non-collisional beam (primary) electrons.[37,38] This would cause an energy spread to the primary population, while the calculated volume averaged primary electron energy is at a reasonable 21 eV.

D. 4R behavior

The 4-ring configuration was an attempt to improve upon the 5R configuration, designed to radially expand the center-line plasma toward the grid plane to achieve better beam flatness. The axial bulk magnetic fields are maintained but designed to diverge downstream with a null region near the grid plane. The furthest downstream ring-cusp is necessary to define the bulk plasma boundary and the isolated electrode prevents loss of primary electrons to the cusp. As previously stated, the performance data from Fig. 8 shows that this configuration was able to achieve high ion current to the grid plane at a given discharge power compared to the 3R and 5R configurations.

The plasma potential map, shown in Fig. 15, reveals that the potential suddenly falls approaching the extraction plane. This plasma structure made it nearly impossible to extract the other plasma parameters from the Langmuir probe sweep. The potential drop is accompanied by a sudden decrease of the electron temperature, reducing the voltage resolution of the data. In addition, the established electric fields led to a spatially dependent accelerated ion population that altered the I–V sweep in an unaccountable manner. The plasma potential delineation is a result of the isolated ring electrode at the cathode potential and the predominately radial magnetic fields. All magnetic field lines downstream of the null region are bounded by cathode biased surfaces that confine the electrons. Therefore, an electric field must be established in order to transport the ions across the field

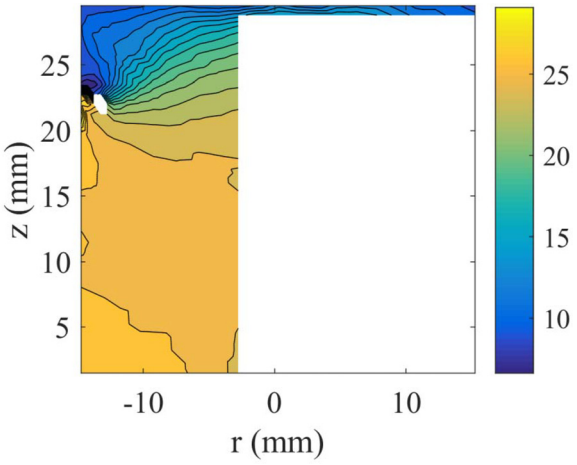

FIG. 15. Plasma potential map of the 4R configuration. The segmented downstream electrodes lead to an internal axial electrostatic field that accelerates the ions from the bulk region to the grid plane.

lines to maintain relative quasi-neutrality. The radially dependent ion velocity distribution would affect the extraction characteristic of the ion optics as they are designed for a low-temperature isotropic ion population. The accelerated ions may lead to impingement of the ion beam against the accelerator grids, causing uneven grid erosion and reducing thruster lifetime.

IV. CONCLUSION

The performance and discharge mapping measurements give crucial insights into discharge behavior of miniature DC ion thrusters. In contrast to larger ion thrusters, these results show that miniature ring-cusp plasma behavior is dominated by the high magnetic fields from the cusps, which leads to high loss rates of high-energy primary electrons to the anode walls. The analyses of the discharge maps confirmed previous findings from computational models on the nature of the MiXI thruster discharge plasma, most notably that the prodigious loss of primary electrons limits the energy transferred to the plasma electrons, such that ions are almost exclusively generated from primary electron ionization. These results are also the first ever experimental validation on the theoretical behavior of the MiXI thruster and miniature ring-cusp discharges.

Primary energy confinement was shown to considerably improve via an imposed axial magnetic field or by using the cathode terminating cusp, resulting in discharge efficiency improvements of up to 50%. For example, results from the 3-ring (3R) and 5-ring (5R) magnetic cusp configuration suggested that almost any cusp exposed directly to the bulk plasma will lead to high primary electron loss. However, findings from the 5R configuration with an axially imposed magnet field indicated that it is possible to well-confine the primary electrons in a miniature discharge without encountering the discharge stability trade-off that has traditionally been considered a driving limitation of the ring-cusp ion thruster design. In addition, the 4-ring (4R) configuration expanded on findings from the 5R configuration and demonstrated very promising improvements to the discharge performance. The use of an isolated ring electrode was found to be

an effective approach to mitigating the primary electron lost at the cusp, but also led to undesirable electric fields within the internal plasma that must be considered in future iterations. Even though these design modifications present some design challenges related to beam flatness and near-grid potentials, they show promise to bypassing the inherent limitations of ring-cusp discharge efficiency at miniature scales.

ACKNOWLEDGMENTS

This work was supported by the Air Force Office of Scientific Research Grant Nos. FA9550-11-1-0029 and FA9550-14-10317 and by the University of California, Los Angeles through the Dissertation Year Fellowship. The authors also acknowledge the valuable contribution of Taylor Matlock for his insights on probe theory and analysis.

[1]R. E. Wirz, J. Mueller, M. Gale, and C. Marrese, in 40th AIAA Joint Propulsion Conference, AIAA Paper 2004-4115, Fort Lauderdale, FL, 2004.
[2]S. Martin, D. Scharf, R. E. Wirz, O. Lay, D. McKinstry, B. Mennesson, G. Purcell, J. Rodriguez, L. Scherr, J. R. Smith, and L. Wayne, in Proceedings of the IEEE Aerospace Conference, Big Sky, MT (2008).
[3]R. Conversano and R. E. Wirz, AIAA J. Spacecr. Rockets **50**, 1035 (2013).
[4]D. M. Goebel and I. Katz, *Fundamentals of Electric Propulsion: Ion and Hall Thrusters* (John Wiley & Sons, New York, 2008).
[5]R. Wirz, S. Araki, and B. Dankongkakul, in *34th International Electric Propulsion Conference,* IEPC-2015-275 (Hyogo-Kobe, Japan, 2015).
[6]J. R. Brophy and P. J. Wilbur, AIAA J. **23**, 1731 (1985).
[7]D. M. Goebel, R. E. Wirz, and I. Katz, J. Propul. Power **23**, 1055 (2007).
[8]K. Leung, N. Hershkowitz, and K. MacKenzie, Phys. Fluids **19**, 1045 (1976).
[9]R. Bosch and R. Merlino, Phys. Fluids **29**, 1998 (1986).
[10]R. Wirz and D. Goebel, Plasma Sources Sci. Technol. **17**, 035010 (2008).
[11]D. A. Herman and A. D. Gallimore, Rev. Sci. Instrum. **79**, 013302 (2008).
[12]A. A. Hubble, J. E. Foster, E. V. Barnat, and B. R. Weatherford, in *33rd International Electric Propulsion Conference, Washington DC,* IEPC-2013-367 (2013).
[13]R. Tsukizaki, I. Toshiyuk, T. Hiroyoshi, K. Nishiyama, and H. Kuninaka, J. Propul. Power **30**, 1383 (2014).
[14]H.-S. Mao and R. E. Wirz, J. Propul. Power **30**, 628 (2014).
[15]R. Wirz, in 41st AIAA Joint Propulsion Conference, AIAA Paper 2005-3887, Tucson, AZ, 2005.
[16]D. A. Herman and A. D. Gallimore, *41st AIAA Joint Propulsion Conference, Tucson, AZ, 2005*, AIAA Paper 2005-4252.
[17]R. E. Wirz, "Discharge plasma processes of ring-cusp ion thrusters," Ph.D. thesis (Caltech, Pasadena, CA, 2005).
[18]D. M. Goebel, Phys. Fluids **25**, 1093 (1982).
[19]J. R. Beattie, "Cusped magnetic field mercury ion thruster," NASA CR–135047 (1976).
[20]J. E. Foster and M. J. Patterson, J. Propul. Power **17**, 428 (2001).
[21]J. R. Brophy, in *21st International Electric Propulsion Conference, Orlando, FL*, IEPC-1990-2655 (1990).
[22]D. M. Goebel, J. E. Polk, and I. G. Mikellides, in *45th AIAA Joint Propulsion Conference, Denver, CO, 2009*, AIAA Paper 2009-4920.
[23]J. E. Foster, A. Hubble, S. Nowak-Gucker, C. Davis, P. Peterson, E. Viges, and D. Chen, in *48th AIAA Joint Propulsion Conference, Atlanta, GA,* AIAA Paper 2012-3795 (2010).
[24]K. Riemann, J. Phys. D: Appl. Phys. **24**, 493 (1991).
[25]R. Wirz, R. Sullivan, J. Przybylowski, and M. Silva, Int. J. Plasma Sci. Eng. **2008**, 693825.
[26]J. Laframboise, "Theory of spherical and cylindrical Langmuir probes in a collisionless, Maxwellian plasma at rest," Ph.D. thesis (University of Toronto, 1966).
[27]F. Chen, Phys. Plasmas **8**, 3029 (2001).
[28]J. Laframboise and J. Rubinstein, J. Phys. Fluids **19**, 1900 (1976).
[29]T. Popov, P. Ivanova, J. Kovačič, T. Gyergyek, and M. Čerček, Plasma Sources Sci. Technol. **21**, 025004 (2012).
[30]Y. Golubovsky, V. Zakharova, V. Pasunkin, and L. Tsendin, Sov. J. Plasma Phys. **7**, 340 (1981).
[31]M. Druyvesteyn, Z. Phys. **64**, 781 (1930).
[32]D. Rapp and P. Englander-Golden, J. Chem. Phys. **43**, 1464 (1965).
[33]M. Hayashi, J. Phys. D: Appl. Phys. **16**, 581 (1983).
[34]E. W. Bell, N. Djurić, and G. H. Dunn, Phys. Rev. A **48**, 4286 (1993).
[35]L. J. Spitzer, *Physics of Fully Ionized Gases* (Interscience Publishers, New York, 1962), pp. 127–135.
[36]D. Rosenburg and G. K. Wehner, J. Appl. Phys. **33**, 1842 (1962).
[37]D. Bohm and E. P. Gross, Phys. Rev. **75**, 1864 (1949).
[38]D. Sydorenko, A. Smolyakov, I. Kaganovich, and Y. Raitses, Phys. Plasmas **14**, 013508 (2007).
[39]B. Dankongkakul and W. E. Richard, "Design of miniature ring-cusp ion thrusters via analysis of discharge EEDF and plasma parameter mapping," 52nd AIAA/SAE/ASEE Joint Propulsion Conference, AIAA Propulsion and Energy Forum, July 25–27 (2016), No. AIAA 2016–4545, pp. 1–14.